# Cold collisions in a laser field: Quantum Monte Carlo treatment of radiative heating

M.J. Holland, K.-A. Suominen, and K. Burnett
*Clarendon Laboratory, Department of Physics, University of Oxford, Parks Road, Oxford OX1 3PU, United Kingdom*
(Received 10 December 1993)

We give a full quantum treatment of the radiative heating mechanism which arises in atomic clouds at low temperatures due to the collisions in the presence of a light field. The time scale of these collisions is comparable to the time scale of spontaneous decay, hence one needs to combine excitation and decay processes with the quantum motion of the colliding atoms into a single model, which we have done. Our study produces a statistical approximate to the full density matrix by combining wave-packet dynamics with the Monte Carlo state-vector method. We also present a quantitative semiclassical treatment based on the Landau-Zener model, and show that it agrees with the quantal results in certain parameter regimes. However, for low temperatures and strong laser fields the full quantum treatment is needed. We describe our numerical procedures and the statistical aspects of the Monte Carlo state-vector method in detail. Our main result is that the low-energy collisions can produce appreciable heating of the cloud.

PACS number(s): 32.80.Bx, 32.80.Pj, 42.50.Vk

## I. INTRODUCTION

Collisions between atoms undergoing laser cooling or trapping limit the densities and temperatures that can be achieved. Establishing the precise limits is, however, an extremely complex matter as one has to treat very cold collisions in the presence of a laser driving field. Due to the extremes of temperatures reached the de Broglie wavelengths involved are very large compared to atomic dimensions. The interactions between the atoms also occur on very large characteristic lengths as the atoms with very little kinetic energy experience their mutual influence at large separations. This means that the quantal motion of the atoms has to be followed on a scale far larger than the one associated with conventional thermal energy collisions [1].

In the presence of the laser driving fields — responsible for the cooling and trapping — an extra complication occurs: excited atoms can emit spontaneously during the slowly evolving collision. This combination of physics means that we have to describe long-range quantal interactions where dissipation is present. This in turn means that we are forced in general to use a density-matrix description of the collision process. There are, however, certain regimes in which semiclassical or perturbative approaches can be used.

The first approach to the problem [2,3] employed a combination of a local excitation model with classical motion on the excited surface. This model, further developed by Julienne and Vigué [4] and by Smith, Burnett, and Julienne [5], was able to give a fairly accurate description of collisions at $T \gtrsim 1$ mK as long as saturation effects could be ignored. The optical Bloch equation (OBE) approach of Band and Julienne [6] remedied the defect in the semiclassical approach for what is now considered a moderately high temperature, i.e., $T \gtrsim 1$ mK. At the very low temperatures now available both these approaches are now known to fail even in the weak-field regime [7,8]. For very weak fields a probe field approach based on optical potentials can be used rather successfully [7]. In the regime we shall address in this paper, namely, ultracold temperatures with laser saturation effects, a full treatment of the density matrix is required and this is what we can now provide [9].

The direct conventional computation of a density matrix for the system of interest is, however, simply not possible with presently available machines [10]. Most fortunately we are now able to produce the equivalent computations using a Monte Carlo state-vector method. This constitutes, we believe, a considerable advance in the field, enabling us to study the long-range collision processes in detail. In this paper we shall study the way in which long-range collisions in a laser field produce heating of the atoms being cooled and trapped. This process exhibits features that cannot be described directly using a semiclassical approach. We have, however, been able to give a description based on the wave-packet dynamics [11] that can be partially explained in semiclassical (Landau-Zener) terms.

The results obtained using our simulation method allow us to make an assessment of the way this collisional heating will affect future experiments. We cannot, of course, include all of the physics responsible for every detail of the collisional process at present. Hyperfine interactions between the entrance and exit channels of the collision will undoubtedly affect the quantitative conclusions. The inclusion of these interactions (which increases the computational problem by three to four orders of magnitude) is part of our ongoing research. In spite of this lack of detail we are able to make considerable progress, particularly in the elucidation of the underlying mechanism of the collisional heating process. We

 

are also able to produce benchmarks for simpler theories that, although more limited in scope, can handle some other aspects of the complexity. In fact, it is *only* through calculations of this type that the limits of the simple theories can be established.

The main result of our study is that low-energy collisions in the presence of a laser field produce appreciable translational heating of the atoms involved. This heating affects the bulk of atoms that participate in collisions. The amount of kinetic energy that a pair picks up is very small compared to that needed to produce trap loss in most practical cases [5,8]. This gain in kinetic energy is, however, very significant when compared to the amount the pair has as they enter the collision. The fact that this heating is significant for the bulk of atoms that participates in collisions also makes possible the simulation of the process using the Monte Carlo state-vector method.

The effects we have been able to describe impinge on the cooling process and limit the temperatures that can be reached at higher densities. This should be contrasted with the fact that most other calculations of cold collision dynamics have focused on trap loss. Computationally collisional heating is a much more complex issue than trap loss as it arises from a nontrivial interplay of excitation and decay. It is, however, exactly the sort of problem the Monte Carlo state-vector method can handle by providing the probability distributions for transitions to occur from initial to final momenta.

The overall effects of the collisional heating process on a particular trapping and cooling scheme will depend on the detailed arrangement of laser fields. We concentrate on a general model for kinetic energy changes at binary collisions and avoid the use of any specific schemes. Our results can then be used in the relevant model of cooling and trapping process to predict the final momentum distributions (or density matrix in quantal treatments) that are reached. This article is organized as follows. In Sec. II we show how one can obtain the Hamiltonian used in our simulations. Wave-packet dynamics and the Monte Carlo state-vector method are presented in Sec. III with an emphasis on the actual numerical implementation. In Sec. IV we present the semiclassical Landau-Zener theory for the heating process. The results from actual simulations for cesium with corresponding predictions of the Landau-Zener approach are presented in Sec. V. Finally, our study is concluded with the discussion of Sec. VI.

## II. THE QUASIMOLECULE COLLISION MODEL

At the moment the atomic densities obtained in magneto-optic traps are in the range $10^9$ cm$^{-3}$ up to $10^{12}$ cm$^{-3}$ [12]. At the low temperatures achievable by laser cooling, the collisions, even though relatively long ranged, can still be regarded as binary events. The time between collisions is several times longer than the spontaneous decay time scale $1/\Gamma$ or the duration of a single collision [13]. All memories of the previous collisions, except possible changes in the kinetic energy, are therefore erased well before the next one is begun. Hence the binary collision approximation (BCA) is well justified and we shall use it. Although we shall describe heating due to collisions, the increase in velocities is not large enough to cause a breakdown of BCA.

We have chosen the cesium two-atom system as the basis of our study. The slowly colliding atoms can be regarded as a quasimolecule system, in which the motion takes place on the corresponding molecular potential surfaces along the axis connecting the two atoms. We can assume for red detunings that our excitation from the $0_g^+$ molecular ground state ($^2S_{1/2}$+$^2S_{1/2}$) occurs dominantly to the attractive $0_u^+$ molecular state ($^2S_{1/2}$+$^2P_{3/2}$) of the $Cs_2$ quasimolecule. The choice of this case is motivated by its potential importance in a wide range of experiments. The method we use is, however, quite general. For simplicity we assume that the ground state is flat with an infinite repulsive core at $R = 0$, where $R$ is the interatomic distance coordinate. The excited-state potential is assumed to consist solely of the dipole-dipole interaction, which dominates the motion on the excited-state surface in the regions important for laser-induced interactions. Hence it has the potential $\hbar\omega_0 - C_3/R^3$, where $\hbar\omega_0$ is the asymptotic energy difference between the ground state and the excited state.

The laser-induced dipole coupling between the molecular states has the classical form

$$V(t) = 2\hbar\Omega\cos(\omega_L t). \tag{1}$$

Both $\Omega$ and the decay parameter $\Gamma$ (introduced later) depend on the dipole moment $d$, and hence on $R$ [4], but for simplicity we ignore this dependence although it can be added when needed. We can also assume that the spatial variation of the field across the region where the field driven dynamics occurs is negligible.

We make a partial-wave expansion of the wave function. Hence for each partial wave with angular quantum number $l$ we have the following radial part:

$$C_g(R,t)\psi_g(\hat{r}_e,R) + C_e(R,t)\psi_e(\hat{r}_e,R), \tag{2}$$

where $\hat{r}_e$ is the set of electron coordinates, and $\psi_g$ and $\psi_e$ are the electronic basis functions in the Born-Oppenheimer approximation. The adiabatic approach to the internal motion of the quasimolecule is justified by the low energies involved. We can assume that the changes in the angular momentum induced by the field have a negligible effect on the wave-packet dynamics. This will hold in the regime we have studied. For substantially lower temperatures or higher couplings this approximation will break down.

In the rotating wave approximation we obtain (in the absence of spontaneous decay) the evolution of the amplitudes to be in the ground and excited states from the time-dependent Schrödinger equation

$$i\hbar\frac{\partial\Psi}{\partial t} = H\Psi, \tag{3}$$

where

$$\Psi = \begin{pmatrix} \Psi_g(R,t) \\ \Psi_e(R,t) \end{pmatrix} = \begin{pmatrix} C_g(R,t)\exp(i\Delta t) \\ C_e(R,t)\exp(i\omega_0 t) \end{pmatrix} \tag{4}$$

and

$$H = \begin{pmatrix} T(R) + U_g(R) & \hbar\Omega \\ \hbar\Omega & T(R) + U_e(R) \end{pmatrix}, \tag{5}$$

with

$$\begin{aligned} T(R) &= -\frac{\hbar^2}{2\mu}\frac{\partial^2}{\partial R^2}, \\ U_g(R) &= \frac{\hbar^2 l(l+1)}{2\mu R^2} - \hbar\Delta, \\ U_e(R) &= \frac{\hbar^2 l(l+1)}{2\mu R^2} - \frac{C_3}{R^3}. \end{aligned} \tag{6}$$

Here the detuning is $\Delta = \omega_0 - \omega_L$ and $\mu$ is the reduced mass of the $Cs_2$ system. The state vector $\Psi(R,t)$ represents the wave packet, which tells us the probability of finding the system at location $R$ at time $t$, and its components $\Psi_g(R,t)$ and $\Psi_e(R,t)$ provide the additional information on the distribution of probability to each state.

The phase shifts introduced in Eq. (4) make the numerical treatment of the problem less tedious by removing rapidly oscillating terms in the time domain. As a result the ground state is shifted up in the energy scale by one laser photon: this is the curve-crossing picture used generally in wave-packet dynamics. In spite of the shift the states are still bare ones. By making the basis transformation into the eigenstates of $H$ (ignoring the kinetic energy operator, though) we obtain the fully field-dressed states, which are often called adiabatic states. They are coupled by the nonadiabatic coupling arising from the spatial derivatives in $H$ — this coupling disappears in the adiabatic limit, which usually corresponds to strong fields and/or slow motion.

The Born-Oppenheimer potential surfaces are occasionally called adiabatic states, but in our terminology they correspond to the bare states, also called diabatic states. Although they are adiabatic in the terms of the internal motion of the quasimolecule on the time scales of the electronic motion, they are diabatic in terms of the laser coupling. Moreover, the spontaneous decay is best defined in terms of the bare states. We have performed our study with bare states in the curve-crossing picture, but occasionally discuss the wave-packet motion also in the terms of the fully field-dressed (adiabatic) states.

## III. WAVE-PACKET DYNAMICS AND MONTE CARLO STATE-VECTOR METHOD

### A. Wave-packet dynamics

In this section we shall describe wave-packet dynamics and the inclusion of dissipation. We discuss our numerical approach, and the details of its implementation. The problems arising from the discretization of position and time in the method are also described.

We shall first discuss the case where spontaneous decay is absent. The art of solving the time-dependent Schrödinger equation (3) with preset initial conditions is generally called wave-packet dynamics [11]. Although some approximate methods can be derived, especially in the semiclassical limit [14], only direct numerical integration of the differential equation itself can yield appropriate solutions.

There are several algorithms available, usually based on the split-operator technique [15], where the Hamiltonian is divided into parts. During one step of time each part operates on the state-vector on its turn. One such division is the separation into the kinetic and potential energy operator parts, as was done in Refs. [10,16]. Another way of splitting the Hamiltonian is based on separating wave-packet motion (WPM) and field-induced interaction (int); we have adopted this approach and write our Hamiltonian as a sum

$$H = H_{\rm WPM} + H_{\rm int}, \tag{7}$$

where

$$H_{\rm WPM} = \begin{pmatrix} T(R) + U_g'(R) & 0 \\ 0 & T(R) + U_e'(R) \end{pmatrix}, \tag{8}$$

$$H_{\rm int} = \begin{pmatrix} -\hbar\Delta & \hbar\Omega \\ \hbar\Omega & 0 \end{pmatrix}; \tag{9}$$

here $T(R)$, $U_e'(R) = U_e(R)$ and $U_g'(R) = U_g(R) + \hbar\Delta$ are as in Eq. (6).

The wave-packet part $H_{\rm WPM}$ will evolve the state-vector components independently along their corresponding potential surfaces, and the interaction part $H_{\rm int}$ provides the laser-induced coupling and detuning. Since the two Hamiltonians commute (we ignore any spatial dependence of the laser field), the integration is treated as a two-step process. The factor $\hbar\Delta$ could alternatively be put into $H_{\rm WPM}$, or even split between the two Hamiltonians. The benefit of this particular operator splitting is that $H_{\rm int}$ is independent of $R$ and $H_{\rm WPM}$ is diagonal.

We start with a given initial condition $\Psi(R,0)$ and advance it for one time step by solving

$$i\hbar\frac{\partial\Psi(R,t)}{\partial t} = H_{\rm WPM}\Psi(R,t), \tag{10}$$

with the Crank-Nicolson method [15,17]. Then, using the resulting $\Psi(R,t)$ as an initial state we solve

$$i\hbar\frac{\partial\Psi(R,t)}{\partial t} = H_{\rm int}\Psi(R,t), \tag{11}$$

with the fourth-order Runge-Kutta algorithm [15]. Then we take the next step in time and repeat the whole process again. In many cases the time scale for the interaction process, set by $\Omega$ and $\Delta$, is much smaller than the time scale for the wave-packet motion. In such cases we can evolve the state-vector for several time steps under $H_{\rm int}$, before applying $H_{\rm WPM}$, thus speeding the numerical integration process. Unfortunately, in our particular problem the time scales for wave-packet motion vary a great deal during the collision process, making such an approach unfeasible.

### B. Monte Carlo simulations

In order to treat the spontaneous decay of the excited state properly one must replace the state-vector $\Psi$ with

the corresponding density operator $\rho$. We can consider the electromagnetic modes of the vacuum as a large reservoir coupled to our system. By applying the standard Markovian approximation (Wigner-Weisskopf) we obtain the reduced system density matrix $\rho(R,t)$. The system dynamics is then given by the Liouville equation

$$i\hbar\frac{\partial\rho}{\partial t} = [H,\rho] - \mathcal{L}[\rho], \tag{12}$$

instead of the Schrödinger equation.

Here $H$ is the Hamiltonian for the nondissipative system; in our case it is given by Eq. (5). The effect of dissipation, i.e., broadening of the excited states and spontaneous decay of populations and coherences, is described by the operator $\mathcal{L}$. For the two-state system this can be written in the form

$$\mathcal{L}[\rho] = i\frac{\hbar\Gamma}{2}(\sigma^+\sigma^-\rho - 2\sigma^-\rho\sigma^+ + \rho\sigma^+\sigma^-), \tag{13}$$

where $\sigma^\pm$ are the standard raising and lowering operators (combinations of Pauli matrices). The factor $\Gamma$ is the decay parameter; in the absence of other processes the excited-state population would decay as $\exp(-\Gamma t)$ (in our study $\Gamma = \Gamma_{\rm mol}$).

One can readily apply Eq. (12) to wave-packet dynamics, but the numerical treatment becomes quite different [10]. Instead of tracking $\Psi(R,t)$ through time we have to work with $\rho(R,R',t)$. If $N_R$ is the number of spatial grid points required for treating $\Psi$ properly, then we need $N_R \times N_R$ points for $\rho$. Even for supercomputers this limits $N_R$ to $10^3$ or less (see Refs. [10,18] for discussion and examples of wave-packet dynamics with density matrix). In brief, one cannot treat our problem with the density-matrix approach, unless an increase of at least two magnitudes in currently available computer memory can be obtained. By using highly oversimplified systems one can use the density-matrix technique to perform studies at temperatures which, unfortunately, are well above those which we want to treat [18].

It is possible to transform Eq. (12) into optical Bloch equations by replacing the quantum dynamics with appropriate semiclassical trajectories, and hence treat cold collision problems [6]. Then spontaneous decay and reexcitation of decayed population are taken into account properly, but the important changes in the kinetic energy due to the spontaneous decay are still left out. In the wave-packet dynamics the divergence of the semiclassical trajectories at classical turning points is unimportant since all motion is treated in a fully quantal way, but in the OBE method one has to adapt the standard WKB approach. It is clear that when $l$ is nonzero and the crossing point and the classical turning point on the ground state lie close to each other, any treatment based on semiclassical trajectories is inadequate. It is clear that we have to keep the quantum motion when treating Eq. (12) with any approximative technique.

The statistical nature of Eq. (12) and spontaneous decay itself can be used as a basis for new methods. Several approaches for obtaining an approximation for the reduced density matrix itself have been developed [19–22]. We have chosen the Monte Carlo wave-function technique proposed by Dalibard, Castin, and Mølmer [21]. It can be easily applied to wave-packet dynamics and has been tested to some extent by comparing it with the corresponding density-matrix approach [10]. Next we shall give a brief and by no means fully comprehensive description of the method; for more details and discussion we refer to Ref. [21].

First, we replace the system Hamiltonian $H$ in the Schrödinger equation with an effective one:

$$H_{\rm eff} = H - i\frac{\hbar\Gamma}{2}\sigma^+\sigma^- = H - i\frac{\hbar\Gamma}{2}\begin{pmatrix} 0 & 0 \\ 0 & 1 \end{pmatrix}. \tag{14}$$

With this Hamiltonian we can take $\Psi(R,t)$ to $\Phi(R,t+\delta t)$; we have used $\Phi$ instead of $\Psi$ to emphasize that since $H_{\rm eff}$ is non-Hermitian, $\Phi$ is not normalized. Indeed,

$$\sum_R \langle\Phi(R,t+\delta t)|\Phi(R,t+\delta t)\rangle = 1 - \delta s, \tag{15}$$

where the sum can be considered either as a summation over the spatial grid, or integration over the spatial continuum, the former being the numerically necessary approximation of the latter.

In the Monte Carlo approach $\delta s$ is the probability of making a quantum jump during the time step $\delta t$ from an excited state to the ground state, followed by a detection of the emitted photon. In a two-state system we have

$$\delta s = \Gamma|\Psi_e(t)|^2\delta t; \tag{16}$$

$|\Psi_e(t)|^2 \equiv \sum_R |\Psi_e(R,t)|^2$ is simply the total excited-state population before the time step is taken.

After having advanced our state-vector with the effective Hamiltonian, we produce a random number $\epsilon$ between 0 and 1. If $\delta s$ is less than $\epsilon$, which is quite probable since $\delta s$ is small, we assume that a quantum jump did not occur. Then we simply proceed by renormalizing our state-vector $\Phi(R,t+\delta t)$ into $\Psi(R,t+\delta t)$ and take the next time step. However, if it occurs that $\epsilon < \delta s$, we assume that a quantum jump did take place. Hence we know that at $t$ the system was in the excited state, and at $t+\delta t$ it is in the ground state. We set $\Psi_e(R,t+\delta t) = 0$ and $\Psi_g(R,t+\delta t) = \Phi_e(R,t+\delta t)$, normalize the new state-vector to unity, and take the next time step.

Following the above procedure we obtain a state-vector with a history of time evolution perturbed by quantum jumps. If we repeat the process, we get a state-vector with a different history, due to the random choice of $\epsilon$. Each state-vector becomes a member in an ensemble, which in the limit of infinite number of members corresponds to the density matrix, see Ref. [21]. However, finite ensembles can give a reasonable approximation for the density matrix. The study presented in Ref. [10] indicates that already ensembles with less than $10^3$ members provide a good approximation for density-matrix wave packets. For reasonably accurate results even ensembles with 50 or so members can be adequate enough; this is also our experience. We shall discuss the appropriate sizes for ensembles further when presenting the actual results.

With the Monte Carlo technique we can now produce an approximation for the density matrix with standard wave-packet dynamics. We add the non-Hermitian part to $H_{\rm int}$. After each internal step we calculate $\delta s'$ and with a random number determine whether a jump occurred or not. Each full integration produces an ensemble member; it is important to notice that if we want to calculate distributions in the momentum space correctly, we must in the end take the average over Fourier-transformed state-vectors, rather than a Fourier transform over the average state-vector. This applies also to taking expectation values for operators which are not $c$ numbers in position or momentum representation.

In wave-packet dynamics it is easy to encounter situations where the decay parameter $\Gamma$ has a spatial dependence. Even in our cold collision study the retardation corrections (large $R$) and Hund's case basis changes (small $R$) produce such an effect. However, as mentioned earlier, we have chosen to neglect them. If they were to be taken into account, we could simply replace Eq. (16) with

$$\delta s = \sum_R \Gamma(R)|\Psi_e(R,t)|^2 \delta t \tag{17}$$

and proceed as usual with $\Gamma = \Gamma(R)$ in Eq. (14).

In the limit of strong coupling $\Omega$ one is tempted to diagonalize the Hamiltonian, and proceed by calculating the time evolution along the field-dressed potential surfaces. It is numerically less demanding, because the new coupling term in the Hamiltonian is rather small, and appears more like a perturbation. However, we would then have a decay factor $\Gamma$ with a strong spatial dependence, and the whole concept of quantum jumps would become rather complicated, as the new states would be combinations of the ground and excited states. Hence we shall always use the bare states as our basis for numerical integration, even in the limit of large coupling.

As described in Ref. [21], the Monte Carlo technique can be adapted to take into account the momentum changes in the system due to the spontaneous emission. A new random element is then added for the direction and polarization of the spontaneously emitted photon. By keeping track of the quantum jumps one can estimate the magnitude of the additional momentum diffusion caused by the random photon emission. However, since we are treating situations with momentum values at least ten times the momentum of recoil, we can ignore it. Besides, it would be inconsistent to add these "momentum kicks" when the similar effect of the laser field is ignored, i.e., $\exp(\pm i\vec{k}\cdot\vec{R})$ terms in the light field.

### C. Scaling and effective potentials

For practical purposes it is best to scale the Schrödinger equation and physical quantities involved. We have chosen the scaling summarized in Table I. Then the classical relations between velocity $v$, momentum $p$, and kinetic energy $E_{\rm kin}$ become

$$v = 2p \quad \text{and} \quad E_{\rm kin} = \frac{1}{4}v^2 = p^2, \tag{18}$$

TABLE I. The physical units (scaling) used in this paper. The key quantity is $k_{\rm rec}$, which is the wave number for the transtion between the ground state and the excited state (at larger $R$) in our model. It also defines our momentum unit as the recoil pick given to an atom by an emitted or absorbed resonant photon. Here $a_o = 5.291\,177$ Å is the Bohr radius and $\mu = 1.1\times10^{-25}$ kg is the reduced mass of the $Cs_2$ system.

| Quantity | Unit | Unit value in $Cs_2$ |
|---|---|---|
| distance | $\lambda\!\!\!^{-} = \lambda/2\pi = 1/k_{\rm rec}$ | 136 nm $= 2560a_0$ |
| momentum | $\hbar k_{\rm rec}$ | $7.78\times10^{-28}$ kg m/s |
| time | $2\mu/\hbar k_{\rm rec}^2$ | 38.5 $\mu$s |
| energy | $(\hbar k_{\rm rec})^2/2\mu$ | $2.74\times10^{-30}$ J |
| velocity | $\hbar k_{\rm rec}/\mu$ | 7.1 mm/s |
| temperature | $(\hbar k_{\rm rec})^2/2\mu k_B$ | 0.2 $\mu$K |

i.e., the reduced mass $\mu$ is in effect equal to 1/2. The values for temperatures associated with the relative motion are obtained from the expression $T = p^2$, in units of 0.2 $\mu$K. The Doppler temperature for $Cs_2$ is $T_D = 130$ $\mu$K, and the corresponding value of $p$ is 26. The maximum initial momentum used in our study is 60 units, corresponding to $T = 0.7$ mK.

The main consequence of adopting these units is that our Schrödinger equation becomes

$$i\frac{\partial}{\partial t}\begin{pmatrix}\Psi_g\\ \Psi_e\end{pmatrix} = \begin{pmatrix}\tilde{T}+\tilde{U}_g & \Omega\\ \Omega & \tilde{T}+\tilde{U}_e\end{pmatrix}\begin{pmatrix}\Psi_g\\ \Psi_e\end{pmatrix}, \tag{19}$$

where

$$T = -\frac{\partial^2}{\partial R^2}, \quad \tilde{U}_g = \frac{l(l+1)}{R^2} - \Delta, \quad \tilde{U}_e = \frac{l(l+1)}{R^2} - \frac{C_3}{R^3}. \tag{20}$$

The above form is extremely suitable for numerical treatment. For our particular $Cs_2$ model we have then $C_3 = 1925$, $\Gamma_{\rm at} = 1240$, and $\Gamma_{\rm mol} = 1655$, corresponding to the values given in Ref. [4] for our system [$\Gamma_{\rm at} = 5.13$ MHz, $\Gamma_{\rm mol} = (4/3)\Gamma_{\rm at}$, and in atomic units $C_3 = 20.33(ea_0)^2$].

Wave packets evolving along the attractive $-C_3/R^3$ potential can have enormous kinetic energies when they reach the distances of a few tens of Bohr radius, where the potentials finally become repulsive. Our numerical methods cannot deal with the corresponding momentum values. However, for the range of detunings we treat we can safely assume that the strong spontaneous decay depletes the excited state before significant kinetic energies are reached. Also, the time which the system would spend at short ranges is small compared with the decay time scales. In any case, since we are interested in the heating rather than trap losses, it is quite adequate to replace $-C_3/R^3$ with a potential which is finite at $R = 0$, but resembles it well at distances above $500a_0$. Such an effective potential is, e.g.,

$$\tilde{U}_{\rm eff}(R) = -\frac{C_3}{(R^n + R_{\rm off})^{3/n}}. \tag{21}$$

We have chosen $R_{\rm off} = 10^{-8}$ and $n = 12$; then $\tilde{U}_{\rm eff}(0) = 100C_3$, and until $R = 0.3$ ($770a_0$) the deviation of $\tilde{U}_{\rm eff}$

from $-C_3/R^3$ remains less than half a percentage, but then increases rapidly as $R$ becomes smaller. For the centrifugal potentials we have just replaced $R$ with $R + R_{\rm off}$, to avoid the singularity at $R = 0$.

### D. Initial conditions

In wave-packet dynamics we need to know the form of the wave packet at the initial moment $t = 0$. We have to abandon the standard scattering theory concepts of probability fluxes with single valued energies, momentums, and directions. In reality we have distributions with finite widths, limited by the Heisenberg uncertainty principle.

We define the initial condition as a minimum uncertainty wave packet:

$$\Psi_g(R,0) = \frac{1}{\sqrt[4]{2\pi(\Delta R_0)^2}} \exp\left[-\frac{(R-R_0)^2}{4(\Delta R_0)^2} + ip_0R\right]. \tag{22}$$

The probability distribution $|\Psi_g(R,0)|^2$ is peaked at $R_0$ and has the full width $\Delta R_0$. The corresponding momentum distribution is

$$P_g(p,0;p_0) = \frac{1}{\sqrt{2\pi(\Delta p_0)^2}} \exp\left[-\frac{(p-p_0)^2}{2(\Delta p_0)^2}\right], \tag{23}$$

with $\Delta p_0\, \Delta R_0 = 1/2$.

When this wave packet evolves freely on the flat ground state it spreads: $\Delta R(t) = \Delta R_0\sqrt{1 + t^2/\Delta R_0^4}$; we call this the free spreading of the wave packet, to make a distinction with the collision-induced diffusion. In order to avoid having a large spatial separation between fast and slow components of the wave packet as it approaches the crossing we need to place it relatively near to the crossing in the beginning. If we solve Eq. (11), with the initial condition $|\Psi_g(0)| = 1$, we obtain

$$|\Psi_g(t)|^2 = \cos^2(\omega t) + \frac{\Delta^2}{4\omega^2}\sin^2(\omega t), \tag{24}$$

$$|\Psi_e(t)|^2 = \frac{\Omega^2}{\omega^2}\sin^2(\omega t), \tag{25}$$

where $\omega = \sqrt{\Delta^2/4 + \Omega^2}$ [23]. One can see these Rabi oscillations in the wave packet as it moves towards the crossing.

When spontaneous decay is turned on, the above picture is changed. The Rabi oscillations will disappear within a few time steps and the population inversion reaches a steady-state value, which is a result of the interplay between the field-induced inversion and spontaneous decay. In the steady state, before the dipole-dipole potential starts to have an effect and the wave packet enters the immediate interaction region, we then have [23]

$$\left(|\Psi_e|^2\right)_{\rm SS} = \frac{\Omega^2}{\Delta^2 + 2\Omega^2 + (\Gamma/2)^2}. \tag{26}$$

One should choose the initial position of the wave packet so that the steady state between practically flat energy surfaces is formed well before entering the crossing region. We have chosen $R \simeq 10^4 a_0$ as the initial position; then $\tilde{U}_{\rm eff}(R_0) = 0.024\Gamma_{\rm at} \ll \Gamma_{\rm at}$.

We propagate our wave packet into the crossing and then wait until all important components have emerged again, i.e., reappeared in the region where the excited-state potential is relatively flat. Normally the interactions near $R \simeq R_{\rm cr}$ cause a large spatial spreading of the wave-packet, which overwhelms the free spreading $\Delta R(t)$. In the end we have all the wave-packet components of importance at large values of $R$, and they once again settle into a steady state given by Eq. (26).

Although our initial and final states are not taken on uncoupled surfaces, they nevertheless correspond to the system starting from and arriving into a well established steady state. Hence we define the collision-induced changes in the kinetic energy as differences between the ground-state momentum distributions corresponding to the observed precollision and postcollision steady states.

### E. Discretization of position and momentum spaces

The fact that we must limit ourselves to a finite, discretized space instead of an infinite continuum requires some discussion. In position space we have a grid with $N_R$ points and constant spacing covering a length of $L$. Hence our spatial resolution is $\delta R = L/(N_R - 1)$. Of course, we would like to minimize $L$ and maximize $N_R$, in order to have good spatial resolution. However, these quantities will also determine our momentum space characteristics: maximum absolute value for available momentum is $|p|_{\rm max} = \pi/\delta R = \pi(N_R - 1)/L$, and resolution is $\delta p = \pi/L$. We restrict the values for $N_R$ to $2^n$, where $n$ is an integer; this speeds up the numerical fast Fourier transform routine.

Since the collision process can spread the initial wave-packet quite a lot in both position and momentum, we need large enough boxes to follow the fast wave-packet components until the slow ones have had enough time to get out of the immediate collision region. Because we are only interested in distributions of absolute values of momentum we can allow the fast components to be reflected at $R = L$, as long as we stop our integration before they have reached the crossing region again. Even this restriction could be lifted; the fast components have a very small excitation probability as they reenter the crossing region. Besides, they usually form only a small fraction of the total population.

We settled in our study with $N_R = 2^{14} = 16\,384$ and $L = 35$, giving $\delta R \simeq 0.0021$. Since our initial wave packet has the width $\Delta R_0 = 0.25$ it is well defined in terms of our spatial grid: $\Delta R_0/\delta R \simeq 120$. Correspondingly, $|p|_{\rm max} \simeq 1470$ and $\delta p \simeq 0.09$, which defines the initial momentum distribution with a reasonable accuracy: $\Delta p_0/\delta p \simeq 22$.

### F. Numerical accuracy

The routines which we use for numerical integration are accurate to second order in the time step $\delta t$. If $E$

represents the largest values of energy involved in our study, then we require that in scaled units $\delta t \ll 1/E$. Hence the phase term $\exp(-iEt)$ is well defined in our time grid. In terms of kinetic energy and momentum this becomes $\delta t \ll p^{-2}$. We have used integration times $T$ from 0.35 to 0.7, with the number of points $N_t = 8192$. Then $\delta t$ becomes equal to $p^{-2}$ roughly at $p \simeq 110$ for $T = 0.7$ and $p \simeq 150$ for $T = 0.35$. This allows us to treat properly the bulk of the collision process, i.e., the heating below $p = 100$, but not necessarily the small fraction of momentum components responsible for trap losses.

The second criterion for $\delta t$ is set by spontaneous decay. We simply require that $\delta t \ll 1/\Gamma_{\rm mol} \simeq 6 \times 10^{-4}$, which is clearly fulfilled even by the largest $\delta t$ used.

The stability of the Crank-Nicolson method requires that $\delta R^2 \leq \frac{\hbar}{2\mu}\delta t$ [15], which in our scaling is simply $\delta R^2 \leq \delta t$. Since for us $\delta R^2 \simeq 4.6 \times 10^{-6}$, the criterion is fulfilled. If both the criterion $\delta t \ll p^{-2}$ and the stability criterion are satisfied, then necessarily $p\delta R \ll 1$ is true, and the wave-function momentum terms such as $\exp(\pm ipR)$ are well defined over the discretized position space.

## IV. THE SEMICLASSICAL APPROACH

### A. The Landau-Zener theory

In this section we present a simple semiclassical method for obtaining the momentum distributions. As the wave packet evolves along a potential surface we can, to some extent, regard it as a classical object moving under the influence of the potential. The idea is to slice the wave packet into a multitude of components, each of which evolves independently according to the Newtonian laws of classical mechanics. The slicing can be done either in position or in momentum representation. Of course, this approach has only limited use, as it clearly cannot describe any processes involving phase effects and genuinely quantum mechanical phenomena.

In the case of two potential surfaces, coupled by some interaction, and possibly brought into resonance as well, the above approach can be connected with purely time-dependent quantum mechanical models, which have analytic solutions [11]. The best known case is the use of the Landau-Zener theory [24] for wave packets moving through a linear level crossing with constant coupling [18,25]. Since most potential surfaces can be safely linearized in the vicinity of crossings, this model can be applied to a number of situations. We shall next give a brief presentation of the Landau-Zener method, and apply it to the cold collision problem.

We start with a purely time-dependent situation. We consider two states, which have energy values that change linearly in time, with a difference $\Delta E = \beta t$, $\beta$ being a constant parameter. These states are degenerate at $t = 0$, and coupled by a constant interaction $\Omega$; they uncouple asymptotically at $t \to \pm\infty$. If we start on one state at $t = -\infty$, then we have the probability

$$\Pi = \exp\left(-\frac{2\pi\Omega^2}{\beta}\right) \tag{27}$$

to be on that state as $t \to \infty$. This is the expression Zener derived by solving the time-dependent Schrödinger equation (which leads to parabolic cylinder functions) and Landau derived using contour integration in the complex time plane, both independently in 1932 [24].

Next, we regard the wave packet in momentum representation to be made of independent momentum components. The wave packet traverses a level crossing at $R = R_{\rm cr}$, formed by linear potential surfaces for which the potential difference is $\Delta\tilde{U} = \tilde{U}_e - \tilde{U}_g \simeq \alpha(R - R_{\rm cr})$. If the change in the motion of the components is negligible during the passage through the level crossing, i.e., the interaction region surrounding the crossing point, we can take a simple classical path $\Delta R = v\Delta t = 2p\Delta t$ for each momentum component. With $\Delta\tilde{U} \simeq 2\alpha p\Delta t$, $2\alpha|p|$ is easily identified with $\beta$ in Eq. (27), and we can write for each component the excitation probability

$$P_{\rm LZ}(p) = 1 - \exp\left(-\frac{\pi\Omega^2}{|p|\alpha}\right). \tag{28}$$

Integration of this result with the incoming wave-packet momentum distribution over $p$ gives the excitation probability of the wave packet [18]. Often Eq. (28) varies very little over the momentum distribution and can be used directly with $p = \langle p \rangle$.

We shall apply this approach to our specific cold collision problem. We limit the discussion in this section to the $l = 0$ case; angular momentum states will be addressed in Sec. V. If we linearize the $-C_3/R^3$ potential at $R = R_{\rm cr}$, we get $\alpha = 3(\Delta^4/C_3)^{1/3}$. In the original Landau-Zener theory the crossing has the natural time scale $\tau_{\rm cr} = 2\Omega/\beta = \Omega/(|p|\alpha)$. This gives the spatial width of the interaction region as $\Delta R_{\rm cr} \simeq 2\Omega/\alpha$. By studying the higher order terms in the Taylor expansion of $-C_3/R^3$ near $R = R_{\rm cr}$ one can set the condition of validity for the linearization of the crossing as

$$\frac{\Omega}{\Delta} \ll 1. \tag{29}$$

It is not surprising that this is also the condition under which the excited-state population in the steady state for large $R$ is small. In Fig. 1 we show the appropriate level structures for the parameter choices studied in Sec. V. In order to visualize the width of the crossing we have also plotted the lower adiabatic state for each case. Except for the ($\Delta = 2\Gamma_{\rm at}$, $\Omega = \Gamma_{\rm at}$) case, the linearization is a valid approximation.

The initial mean momentum $p_0$ is the main factor in determining if the incoming wave packet traverses the crossing adiabatically, i.e., if it follows the lower adiabatic surface rather than the bare states. The slower the wave packet is, the more time it has to get excited. In Fig. 2 we plot Eq. (28) as a function of momentum for selected parameters; we use the notation $(m, n)$ for different parameter combinations: $\Delta = m\Gamma_{\rm at}$ and $\Omega = n\Gamma_{\rm at}$. Clearly, with values of $|p_0|$ close to 10 units the wave packet evolves and moves onto the excited state adiabat-

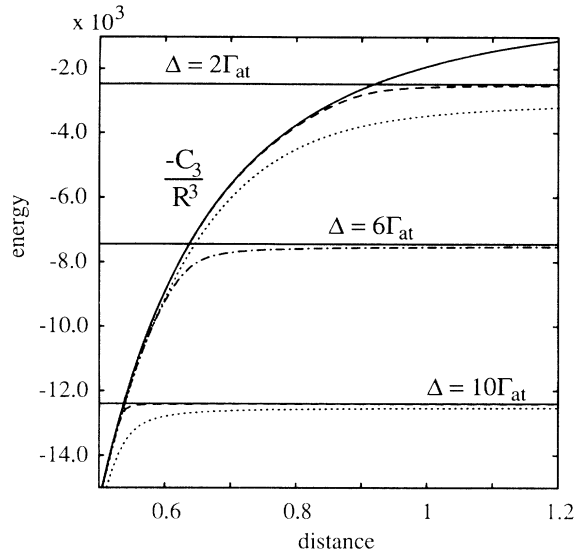


FIG. 1. The level configurations for the chosen combinations of detuning $\Delta$ and coupling $\Omega$ in the curve-crossing picture. We have plotted the smaller eigenvalue of the Hamiltonian in Eq. (19) in order to demonstrate the size of the interaction region. The dotted lines are for $\Omega = \Gamma_{at}$, the dashed lines for $\Omega = 0.2\Gamma_{at}$, and the dot-dashed line for $\Omega = 0.6\Gamma_{at}$. The flat solid lines represent the ground-state positions for different detunings, and the curved solid line stands for the excited-state potential surface.

ically as it passes through the interaction region. However, if it is strongly accelerated by the radiative heating mechanism, it has a clear nonzero probability to remain in the ground state when it goes through the crossing for a second time after a reflection at the core. Also, the $-C_3/R^3$ potential is less steep for $R > R_{cr}$ than for

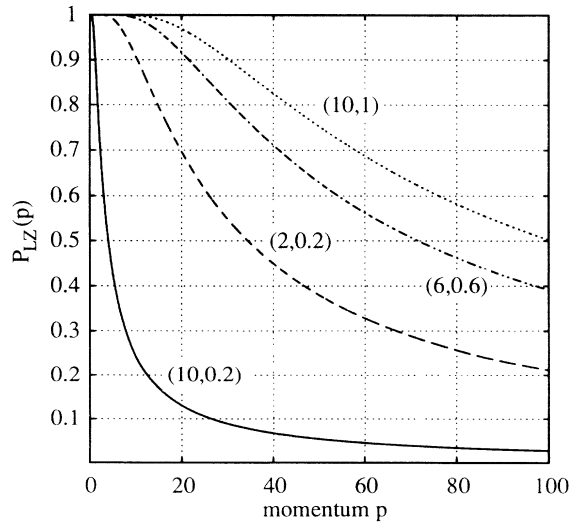


FIG. 2. The momentum dependence of the Landau-Zener transition probabilities. The crossing process is adiabatic when $P_{LZ}$ is close to unity. In the (2,1) case $P_{LZ}$ is practically equal to unity for $p < 100$, and is therefore omitted. The lines correspond to the different (detuning,coupling) combinations as marked in the graph.

$R < R_{cr}$, especially if the detuning is small. Because of these asymmetries it is possible to observe heating as a net effect (a clear shift in the mean value of momentum), in addition to diffusion (increase in the width of the momentum distribution). Since we have spontaneous decay in our model, any phase information from the first crossing is wiped out before the second one is entered. Hence effects such as Stückelberg oscillations are absent; however, they do exist in nondissipative wave-packet dynamics [26].

In the limit of weak dissipation the spontaneous decay acts mainly after the excitation process rather than during it. This is not true for ultracold collisions; we shall discuss them later. By assuming a purely resonant excitation ($\Delta R_{cr} = 0$), we can write a relation between time $\tau$ spent on the excited state and obtained momentum change, if the system experiences a quantum jump back to the ground state at $\tau$. The probability distribution for a quantum jump taking place during the interval $[\tau, \tau + d\tau]$ is simply

$$P_j(\tau) = \Gamma \exp(-\Gamma\tau) d\tau. \tag{30}$$

The classical path approximation for the first entry into the crossing gives

$$\begin{aligned}\tau &= \int_{R_{cr}}^{R} \frac{dR'}{2p(R')} \\ &= -\int_{R_{cr}}^{R} \frac{dR'}{2\sqrt{p_{cr}^2 + C_3/R'^3 - \Delta}},\end{aligned} \tag{31}$$

where $p_{cr}$ is the momentum of the wave packet (or its component) when it enters the crossing. At this point we define for simplicity all momentum values to be positive, even when the motion takes place from large values of $R$ towards smaller ones. Using Eqs. (30) and (31) we obtain the distribution in momentum terms:

$$\begin{aligned}P_j(p) = \frac{\Gamma}{\alpha}\left(1 + \frac{p^2 - p_{cr}^2}{\Delta}\right)^{-4/3} \\ \times \exp\left[-\frac{\Gamma}{\alpha}\int_{p_{cr}}^{p} dp' \left(1 + \frac{p'^2 - p_{cr}^2}{\Delta}\right)^{-4/3}\right] dp.\end{aligned} \tag{32}$$

This expression, if integrated over $p_{cr}$ with the distribution of $p_{cr}$, is in fact the momentum distribution we expect to find on the ground state when all the population on the excited state has finally disappeared. Similarly, swapping $p$ ($p'$) and $p_{cr}$ in Eq. (32) we obtain an expression valid for the second crossing.

If we take the spontaneous decay to be too weak to interfere with the excitation process, but so strong that most of the decay takes place while the linear approximation is valid, Eq. (32) becomes very simple with $p(\tau) = \alpha\tau + p_{cr}$:

$$P_j(p) \simeq \frac{\Gamma}{\alpha} \exp\left[-\frac{\Gamma}{\alpha}(p - p_{cr})\right] dp. \tag{33}$$

A model for radiative heating must involve the two sequential level crossings. The first one occurs as the

initial wave packet on the ground state enters the interaction region. The second one is encountered by the core-reflected outcoming wave packet. We can separate four cases: (a) no excitation at all, (b) excitation and decay only at the first crossing, (c) excitation and decay only at the second crossing, and (d) excitation and decay at both crossings. We assume that Eq. (33) can be applied instead of Eq. (32).

The first crossing accelerates the wave packet ($p \geq p_{\rm cr}$), and the second one decelerates it ($p \leq p_{\rm cr}$). In the linear approximation the asymmetry causing net heating is provided by Eq. (28). Then, following the guidelines of previous discusssion we obtain for the final ground-state momentum distribution the expression

$$P_f(p,p_0) = [1-P_{\rm LZ}(p)]^2 P_g(p,0;p_0) + \frac{\Gamma}{\alpha}[1-P_{\rm LZ}(p)]\exp(-\Gamma p/\alpha)\int_0^p dp' \exp(\Gamma p'/\alpha) P_{\rm LZ}(p') P_g(p',0;p_0)$$
$$+\frac{\Gamma}{\alpha}\exp(\Gamma p/\alpha)\int_p^\infty dp' \exp(-\Gamma p'/\alpha) P_{\rm LZ}(p')[1-P_{\rm LZ}(p')] P_g(p',0;p_0)$$
$$+\frac{\Gamma^2}{\alpha^2}\exp(\Gamma p/\alpha)\int_p^\infty dp'' \exp(-2\Gamma p''/\alpha) P_{\rm LZ}(p'')\int_0^{p''} dp' \exp(\Gamma p'/\alpha) P_{\rm LZ}(p') P_g(p',0;p_0). \quad (34)$$

The four terms correspond to the cases (a)–(d) mentioned above, in that order. This distribution is for absolute momentum, i.e., we use positive $p$'s for both incoming and outgoing cases. For the results given in Sec. V we have used Eq. (23) for $P_g(p,0;p_0)$, and $\Gamma = \Gamma_{\rm mol}$.

With the above expression (34) one can try to bridge the gap between the wave-packet dynamics subjected to the Heisenberg uncertainty principle, and standard stationary scattering theory in which single momentum and single energy states are allowed (since we look at infinite time). By exchanging the Gaussian initial distribution for a Dirac $\delta$ function one obtains a mapping from single initial $p_0$ to single final $p$ — a true scattering matrix.

As usual, there is a snag: we can expect Eq. (34) to work only in a narrow region of parameter space. First, the linearization argument must be valid for both the Landau-Zener result and the classical path [Eq. (33)]. Secondly, our assumption of only four possible cases (a)–(d) can be questioned. If the second crossing remains highly adiabatic for the outcoming wave packet, and if it does not possess enough kinetic energy to escape the potential well formed by the reflective core at $R = 0$ and the excited-state potential, it may be trapped. Eventually the wave packet escapes either by experiencing a quantum jump near its outer turning point, or by tunneling out via a nonadiabatic transition at the crossing.

### B. Population recycling

In this subsection we consider the main complication in the Landau-Zener approach, which arises when the spontaneous decay is strong, i.e., quantum jumps are likely to take place when the wave packet is still going through the excitation process. Then Eq. (34) should fail as jumps are followed by an almost immediate reexcitation; it is called population recycling. In Fig. 3 we show the ratio of the time it takes to traverse the crossing ($p$ unchanged during the process) to the mean decay time $1/\Gamma$. If this ratio is larger than one, we can expect recycling of population between the ground state and the excited state during the crossing process.

It is possible to estimate the magnitude for the recycling contribution in the final $\langle p \rangle$. We take the relevant width of the crossing region to be roughly $\Delta R'_{\rm cr} \simeq \Omega/\alpha$, a factor of 2 less than earlier; then our estimate should form a lower limit for the momentum shift. We can assume that while the wave packet is within the interaction region, recycling will effectively keep it in the excited state. The crossing process can be regarded as fully adiabatic if $\Omega$ is large enough compared to other factors: $P_{\rm LZ} = 1$. For large detunings the linearization procedure is still quite valid, so acceleration depends only on the time spent on the excited state, even if the excitation takes place at $R \neq R_{\rm cr}$ (off-resonant excitation due to the power broadening).

Classically, the recycling lasts for $\tau'_{\rm cr}$:

$$\Delta R'_{\rm cr} = 2p_0\tau'_{\rm cr} + \alpha(\tau'_{\rm cr})^2, \quad (35)$$

which gives

$$\tau'_{\rm cr} \simeq \frac{\sqrt{\Omega}}{\alpha}, \quad (36)$$

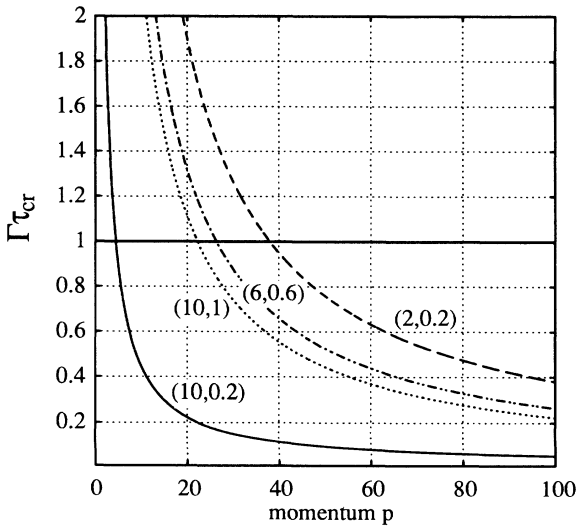


FIG. 3. The ratio of the crossing time $\tau_{\rm cr}$ to the averaged decay time $1/\Gamma$ for different parameter combinations. In the (2,1) case $\Gamma\tau_{\rm cr} \gg 1$ for $p < 100$ and is therefore beyond the range used in the graph. The line styles are as in Fig. 2.

if $\Omega \gg p_0^2$. The wave packet accelerates steadily during the recycling process and we obtain $\Delta\langle p\rangle \sim \alpha\tau'_{\rm cr} \simeq \sqrt{\Omega}$. This shift is independent of $\Delta$, $p_0$, and $\Gamma$.

The recycling process ends when the excitation dies off, and we are left with the normal exponential decay. It produces a second shift $\Delta\langle p\rangle \sim \alpha/\Gamma$ calculated with Eq. (33). Combining the recycling and exponential decay contributions we get the estimate

$$\langle p\rangle \sim \sqrt{\Omega} + \alpha/\Gamma + p_0$$
$$\simeq \sqrt{\Omega} + \alpha/\Gamma, \tag{37}$$

as we have already assumed $\sqrt{\Omega} \gg p_0$. Hence in the (6,0.6) and (10,1) cases we expect to see a large shift in $\langle p\rangle$, which at small $p_0$ is independent of $p_0$. In Table II we show the relevant data regarding the recycling effect and the exponential decay for the parameter combinations used in Sec. V.

Our result is only a rough estimate with limited validity, but it serves well as a reasonable qualitative picture of the wave-packet processes when $\Gamma$ is large and the pure Landau-Zener approach fails. The results presented in Ref. [18] (Figs. 7 and 8) support our analysis of the recycling effect. There the wave packet experiences a large shift in $\langle p\rangle$, which is reduced as $\Gamma$ increases, but still remains relatively large. The corresponding time-dependent data for $\langle p\rangle$ and $\Delta p$ show the formation of a steady state with a lifetime roughly independent of $\Gamma$ for large $\Gamma$, before the exponential decay takes over. The results seem to follow roughly our estimate for recycling [since in Ref. [18] $p_0 \gg \Delta\langle p\rangle$ one has to use the exact solution of Eq. (35) for $\tau'_{\rm cr}$].

It is possible to consider that during recycling only a fraction of the population can simultaneously be on the excited state, in the spirit of Eq. (26). Then, although all wave-packet components experience excitation, they do it effectively only for time $\gamma\tau'_{\rm cr}$, where $\gamma$ is the degree of excitation given by Eq. (26) with a suitable average local detuning. In the case of large $\Omega$ this would increase $\tau'_{\rm cr}$ by a factor of $1/\gamma$, which compensates exactly the diminished acceleration: $\Delta\langle p\rangle \sim \alpha\gamma\tau'_{\rm cr}$. This compensation is not present if $\Delta\langle p\rangle \ll p_0$. The estimates for $\Delta\langle p\rangle$ given by this fractional recycling picture, however, seem to fall clearly below the actual numerical results featured in Ref. [18].

TABLE II. The momentum shifts predicted by the semiclassical approach. The fourth column corresponds to the recycling effect and the fifth one to the exponential decay; their sum appears in the sixth column.

| $\Delta$ | $\Omega$ | $\alpha$ ($10^3$) | $\sqrt{\Omega}$ | $\alpha/\Gamma$ | $\Delta\langle p\rangle$ |
|---|---|---|---|---|---|
| 2 | 0.2 | 8.1 | 16 | 5 | 21 |
| 2 | 1.0 | 8.1 | 35 | 5 | 40 |
| 6 | 0.6 | 35.0 | 27 | 21 | 48 |
| 10 | 1.0 | 69.0 | 35 | 42 | 77 |

## V. SIMULATIONS WITH CS

### A. Simulation results

In this section we present our main results, obtained from the fully quantal approach and from the Landau-Zener approach. First, in this subsection, we look at the $s$-wave scattering, i.e., the case when $l = 0$. We have performed simulations with five different combinations of detuning and coupling strength. We use again the notation $(m,n)$ for $\Delta = m\Gamma_{\rm at}$ and $\Omega = n\Gamma_{\rm at}$. The ensemble sizes were $N \simeq 50$ and above: we shall discuss the ensemble statistics in a later subsection. Here we concentrate on the actual results and their interpretation in the context of the Landau-Zener approach and the recycling effect. In each series of simulations we started with an initial momentum $p_0 = 10$, and increased it in steps of 5 units, until interesting effects disappear or we get to value $p_0 = 60$.

In Fig. 4 we show the excited-state population as a function of time for $p_0 = 10$ (a) and $p_0 = 35$ (b). In all cases the two-state wave-packet system rapidly reaches the steady state, where the population is given by Eq. (26). At the end of the simulation the same steady state reappears. In our calculations the final momentum distributions were taken at larger values of time than those presented in Fig. 4 to assure that even when $p_0$ is small, all components have emerged from the crossing region. This includes any population temporarily trapped into the upper adiabatic state potential well at $R \lesssim R_{\rm cr}$. Except for the (10,0.2) case where the interaction region is very narrow, it is difficult to distinguish at $p_0 = 10$ the double crossing nature of the dynamic process. This is

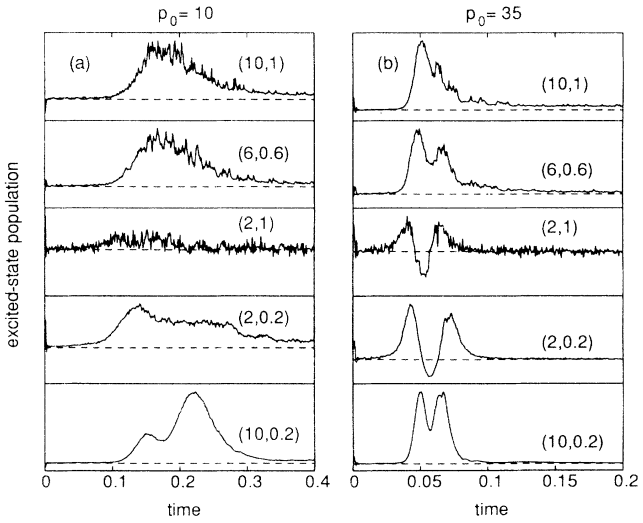


FIG. 4. Examples of the time evolution of the excited-state population as seen in the simulations. Two values for initial momentum are chosen: $p_0 = 10$ for (a) and $p_0 = 35$ for (b). The parameters used are indicated on the figure. The dashed lines correspond to the steady-state populations given by Eq. (26), and they are, from top to bottom, $9.76 \times 10^{-3}$ (10,1), $9.69\times10^{-3}$ (6,0.6), 0.155 (2,1), $8.84\times10^{-3}$ (2,0.2), and $3.98\times10^{-4}$ (10,0.2). The solid bottom line for each individual population graph corresponds to the zero level.

because the initial wave packet has ample time to spread freely in position space before entering the crossing, and a long-lasting mixture of incoming and outgoing components is formed at the interaction region. In the case of $p_0 = 35$ the two crossings are separated by a ditch in population, due to the relatively small precollision free diffusion of the wave packet (it leads to a partial separation in time between the incoming and outgoing wave packets at the crossing).

In Fig. 5 we give two examples of how the wave packet evolves for the (6,0.6) case. In (a), the initial wave packet spreads while moving towards the crossing, goes through the heating process, and returns with a spread that extends well beyond the free one. A part of the wave packet remains trapped in the upper adiabatic state potential well. The trapped population appears as a tall but narrow peak: its weight is very small if compared with the large main part of the wave packet. In (b) the wave packet moves fast and spreads very little before entering the crossing. Since the crossing is not fully adiabatic at $p_0 = 50$, the initial wave packet forms a visible part of the final wave packet. The total diffusion of the wave packet, however, still clearly exceeds the free spreading.

Examples of the wave-packet evolution in the momentum representation are shown in Fig. 6 for the two

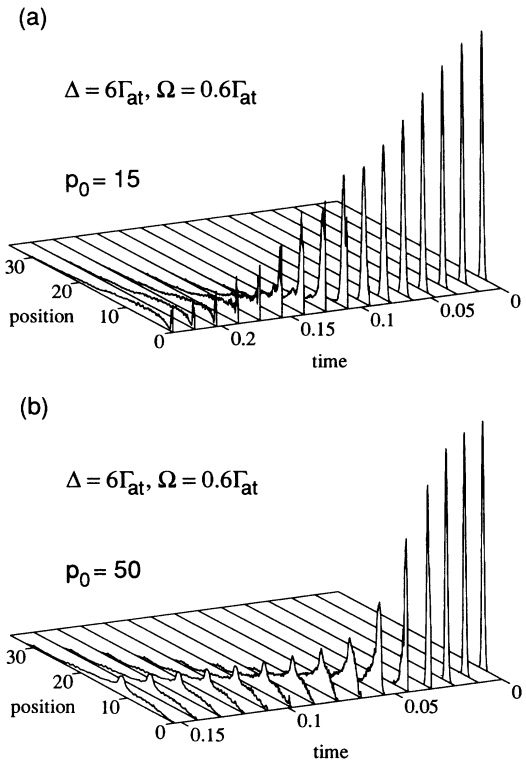


FIG. 5. Examples of wave-packet evolution on the ground state in the position representation. The parameters are as indicated in the figure. The initial Gaussian wave packet is located at $R = 4$ and moves towards $R = 0$ with initial momentum $p_0$. It enters the main collision region ($R < 1$) and then reemerges, except in (a) for the part that is trapped at $R < R_{cr}$ [which eventually escapes later, but in (a) the time evolution is plotted only up to $\tau = 0.24$ in order to show the details of the dominating collision process].

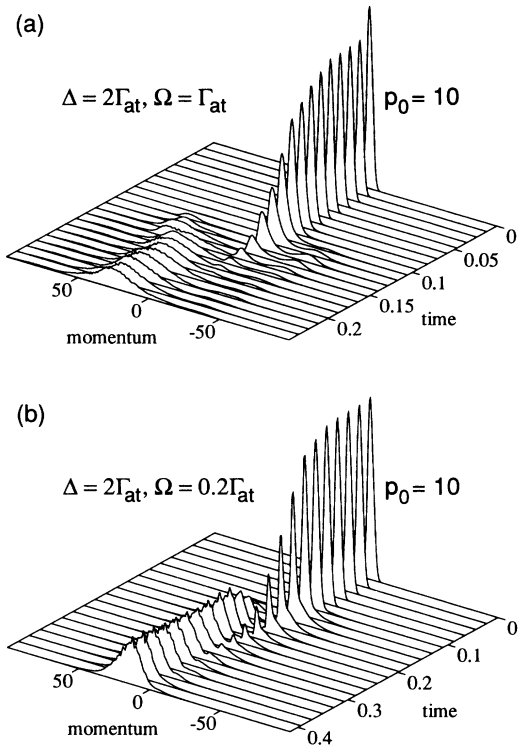


FIG. 6. Examples of wave-packet evolution on the ground state in the momentum representation. The parameters are as marked in the graph. The initial Gaussian wave packet is located at $\langle p \rangle = -p_0$, but the crossing process severely alters its shape and position. In the absence of the coupling to the excited state the initial distribution would merely shift smoothly to $\langle p \rangle = p_0$ and regain its shape, as the wave packet in the position representation is reflected by the repulsive core at $R = 0$.

$\Delta = 2\Gamma_{at}$ cases with $p_0 = 10$. In both figures we see how the sharp initial distribution is depleted as its components experience excitation and core reflection. In (a) the heating clearly dominates as the excitation process is practically adiabatic, and we see peaks appearing in the momentum distribution well separated from the initial value: Eq. (37) gives $\Delta\langle p \rangle + p_0 \simeq 50$, which seems to be an adequate estimate. The core-reflected components reappear at $p > 0$ and eventually move towards smaller values of $|p|$. This is because of deceleration at the second crossing, which is still adiabatic. The net effect is clear heating combined with strong diffusion: we have $\langle p \rangle \simeq 30$, compared with $p_0 = 10$. Since in the (2,1) case the crossing is highly adiabatic even at large $|p|$, the asymmetry needed for the net heating is due to the asymmetry of the $-C_3/R^3$ potential in the vicinity of $R = R_{cr}$.

In Fig. 6(b) we see only slight heating and mainly diffusion as expected from Table II for the (2,0.2) case. At the first crossing the initial wave packet obtains only a small tail towards higher $|p|$, signifying very modest heating (kinetic energy increases only by a factor of 3). Because of the smaller heating, the collision lasts longer than in

the corresponding (2,1) case of Fig. 6(a).

We show in Figs. 7–11 the main results of our simulations, namely, the final momentum distributions. The accompanying numerical data are in Tables III–VI. In general we have calculated the final mean values $\langle p \rangle$ of the distributions using the data up to $p = 100$. For technical reasons stated earlier the accuracy of simulation data above momentum values of $p = 100$ can be questioned. Also, in real experiments one has a limit where heating turns into a trap loss process, determined by the particular setup. Hence there is a real cutoff at some relatively high momentum if only heating is studied. However, in the (10,1) case the contributions from values higher than 100 units are relatively large, and we have included them nevertheless in Table VI. The relative kinetic energy change is expressed with

$$\Delta w = \frac{\langle p^2 \rangle - [p_0^2 + (\Delta p_0)^2]}{p_0^2 + (\Delta p_0)^2}. \tag{38}$$

The case (10,0.2) is not very interesting, as seen from Fig. 7. Only at very small values of $p_0$ does a tiny tail representing partial heating appear. Following Fig. 2 the negligible heating is not a real surprise, as the crossing is not very adiabatic even at $p_0 = 10$. The Landau-Zener results are not shown in the figure. They do, however, predict the tails nicely, but the main parts differ strongly from the simulation results at $p_0 \leq 15$. We shall return to this case when discussing the simulation statistics.

In the case (2,0.2) (Fig. 8) the excitation probability is clearly larger than for (10,0.2) and we observe modest heating (see Table III) for small $p_0$. The Landau-Zener prediction is not too far off, especially at $p_0 \gtrsim 20$. For $p_0 \lesssim 20$ the increase in $\langle p^2 \rangle$ is larger than 100%, and we see in $\langle p \rangle$ minor manifestations of the recycling effect. The use of true semiclassical trajectories, i.e., Eq. (32) does not improve the Landau-Zener result (we tested it).

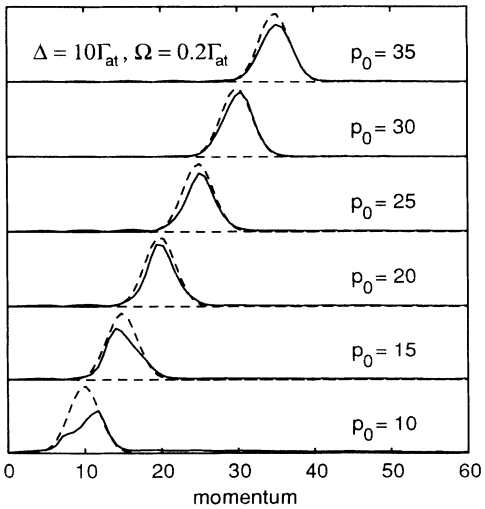


FIG. 7. The final momentum distributions for the (10,0.2) case. The momentum values are as indicated on the graph. The solid line shows the simulation results, and the dashed line is the initial distribution, both normalized to have the same area.

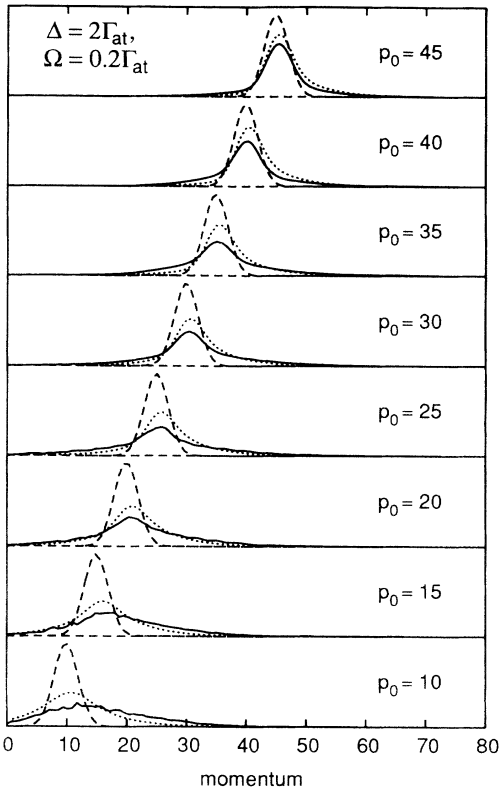


FIG. 8. The final momentum distributions for the (2,0.2) case. The momentum values are as indicated on the graph. The solid lines show the simulation results, the dashed lines the initial distributions, and the dotted ones the corresponding Landau-Zener predictions by Eq. (33). The distributions are normalized to have the same area.

Figure 9 shows a clear breakdown of the Landau-Zener argument for all values of momentum in the (2,1) case. Because of the strong adiabaticity the recycling effect is present at both crossings. But, as discussed in the context of Fig. 6(a), a net heating is present. According to Table IV $\langle p \rangle \simeq 30$ for $p_0 \lesssim 30$. For larger $p_0$ the values for $\langle p \rangle$ simply follow $p_0$. The main failure of the Landau-Zener approach at large $p_0$ is the prediction for spreading.

TABLE III. The simulation and semiclassical data for the (2,0.2) case. The expectation values for the simulation data (the second and the fourth column) and for the Landau-Zener approach (the third and the fifth column) are calculated from the corresponding distributions with a cutoff set to 100 momentum units. The ensemble size is $N$, averaged number of quantum jumps per ensemble member is $\bar{n}$, and the corresponding standard deviation is $\Delta n$.

| $p_0$ | $\langle p \rangle$ | $\langle p \rangle_{LZ}$ | $\Delta w$ | $\Delta w_{LZ}$ | $N$ | $\bar{n}$ | $\Delta n$ |
|---|---|---|---|---|---|---|---|
| 10 | 16 | 12 | 2.6 | 0.8 | 100 | 13.3 | 4.0 |
| 15 | 20 | 17 | 1.2 | 0.4 | 48 | 9.1 | 3.3 |
| 20 | 23 | 22 | 0.6 | 0.3 | 60 | 8.8 | 3.7 |
| 25 | 27 | 27 | 0.3 | 0.2 | 51 | 6.8 | 2.6 |
| 30 | 32 | 32 | 0.3 | 0.2 | 97 | 7.0 | 2.4 |
| 35 | 37 | 37 | 0.2 | 0.1 | 51 | 6.7 | 2.7 |
| 40 | 39 | 42 | 0.0 | 0.1 | 81 | 5.6 | 2.5 |
| 45 | 44 | 47 | 0.0 | 0.1 | 52 | 5.2 | 2.4 |

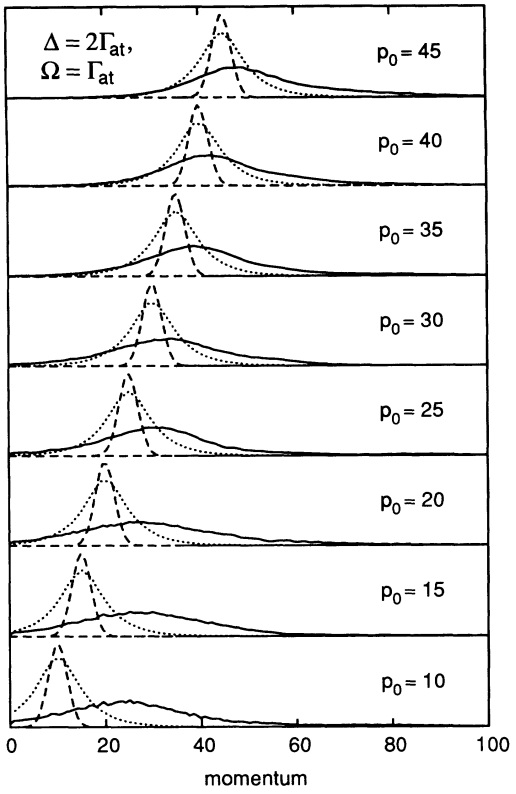


FIG. 9. The final momentum distributions for the (2,1) case. The layout is as in Fig. 8.

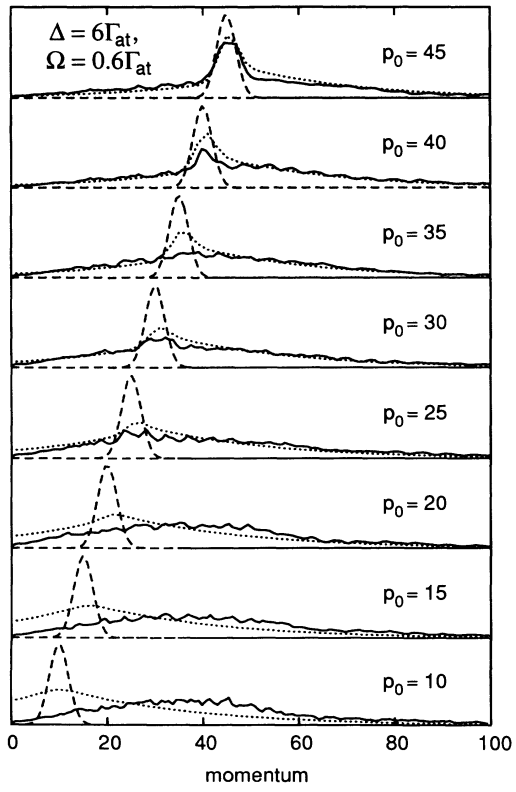


FIG. 10. The final momentum distributions for the (6,0.6) case. The layout is as in Fig. 8.

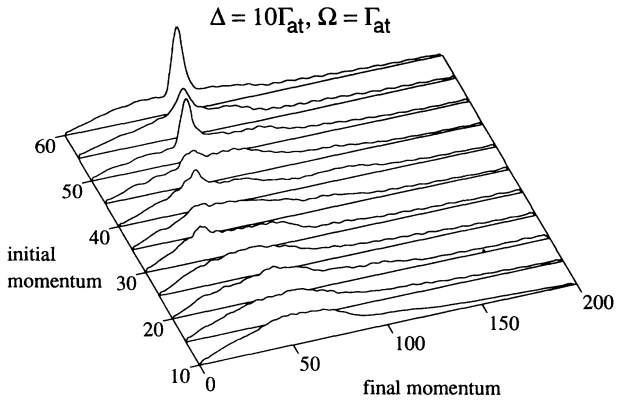


FIG. 11. The final momentum distributions for the (10,1) case as a three-dimensional plot, showing the approximate mapping from initial momentum states to final momentum states. The curves have been smoothed in order to remove the spiky structure due to the small ensemble sizes (the sharp distribution peaks corresponding to the individual ensemble members are smoothed out only in truly large ensembles, with $N \gtrsim 500$ [10]). This procedure improves the visibility of the main characters of the distribution, such as the formation of the long tail at $p > 100$, emergence of the peak at $p_0$ for $p_0 \geq 30$, and the largely $p_0$-independent behavior of the main part located at $p < 100$.

TABLE IV. The simulation and semiclassical data for the (2,1) case. The presentation is the same as in Table III.

| $p_0$ | $\langle p \rangle$ | $\langle p \rangle_{LZ}$ | $\Delta w$ | $\Delta w_{LZ}$ | $N$ | $\bar{n}$ | $\Delta n$ |
|---|---|---|---|---|---|---|---|
| 10 | 28 | 11 | 10.0 | 0.5 | 56 | 140 | 17 |
| 15 | 30 | 16 | 4.0 | 0.2 | 92 | 139 | 13 |
| 20 | 31 | 20 | 2.2 | 0.1 | 51 | 137 | 12 |
| 25 | 33 | 25 | 1.1 | 0.1 | 50 | 113 | 12 |
| 30 | 34 | 30 | 0.5 | 0.1 | 51 | 107 | 15 |
| 35 | 41 | 35 | 0.6 | 0.0 | 59 | 93 | 17 |
| 40 | 45 | 40 | 0.4 | 0.0 | 40 | 94 | 13 |
| 45 | 52 | 45 | 0.4 | 0.0 | 58 | 95 | 17 |
| 50 | 57 | 50 | 0.4 | 0.0 | 50 | 98 | 12 |
| 55 | 60 | 55 | 0.2 | 0.0 | 50 | 93 | 10 |
| 60 | 64 | 60 | 0.2 | 0.0 | 60 | 91 | 12 |

TABLE V. The simulation and semiclassical data for the (6,0.6) case. The presentation is the same as in Table III.

| $p_0$ | $\langle p \rangle$ | $\langle p \rangle_{LZ}$ | $\Delta w$ | $\Delta w_{LZ}$ | $N$ | $\bar{n}$ | $\Delta n$ |
|---|---|---|---|---|---|---|---|
| 10 | 41 | 26 | 20.0 | 9.7 | 53 | 12.3 | 4.0 |
| 15 | 42 | 29 | 8.9 | 4.6 | 80 | 11.8 | 4.8 |
| 20 | 40 | 32 | 4.1 | 2.7 | 51 | 12.2 | 4.6 |
| 25 | 42 | 36 | 2.6 | 1.7 | 55 | 9.8 | 3.7 |
| 30 | 42 | 40 | 1.5 | 1.2 | 51 | 10.2 | 3.8 |
| 35 | 45 | 44 | 1.0 | 0.9 | 51 | 9.3 | 3.8 |
| 40 | 49 | 48 | 0.8 | 0.7 | 56 | 8.0 | 3.6 |
| 45 | 48 | 52 | 0.3 | 0.5 | 50 | 8.2 | 3.8 |
| 50 | 51 | 56 | 0.2 | 0.4 | 58 | 7.8 | 3.7 |
| 55 | 53 | 60 | 0.1 | 0.3 | 78 | 7.2 | 3.0 |
| 60 | 62 | 64 | 0.1 | 0.2 | 56 | 7.8 | 3.2 |

TABLE VI. The simulation and semiclassical data for the (10,1) case. The presentation is the same as in Table III, except that we also give the expectation values calculated from the simulation data with a cutoff placed at 200 momentum units (the second and the fifth column).

| $p_0$ | $\langle p\rangle_{200}$ | $\langle p\rangle$ | $\langle p\rangle_{\rm LZ}$ | $\Delta w_{200}$ | $\Delta w$ | $\Delta w_{\rm LZ}$ | $N$ | $\bar{n}$ | $\Delta n$ |
|---|---|---|---|---|---|---|---|---|---|
| 10 | 69 | 52 | 37 | 63.0 | 31.0 | 19.0 | 52 | 12.9 | 4.1 |
| 15 | 70 | 52 | 39 | 28.0 | 13.0 | 8.6 | 56 | 14.3 | 6.0 |
| 20 | 75 | 52 | 41 | 18.0 | 7.3 | 4.8 | 51 | 15.8 | 7.1 |
| 25 | 70 | 50 | 43 | 10.1 | 4.9 | 3.0 | 51 | 10.7 | 4.9 |
| 30 | 68 | 48 | 46 | 6.4 | 2.2 | 2.0 | 52 | 11.9 | 6.2 |
| 35 | 69 | 51 | 48 | 4.4 | 1.6 | 1.4 | 49 | 9.8 | 4.6 |
| 40 | 73 | 51 | 51 | 3.5 | 0.9 | 1.0 | 61 | 10.4 | 6.2 |
| 45 | 72 | 55 | 54 | 2.3 | 0.8 | 0.7 | 50 | 9.4 | 4.9 |
| 50 | 74 | 50 | 56 | 1.9 | 0.5 | 0.5 | 56 | 9.9 | 5.2 |
| 55 | 73 | 55 | 59 | 1.4 | 0.2 | 0.3 | 51 | 9.2 | 4.3 |
| 60 | 72 | 56 | 62 | 0.9 | 0.0 | 0.2 | 54 | 9.3 | 4.7 |

The linearization argument is far from valid for both the excitation process and the semiclassical trajectory since the levels do not decouple at $R \gg R_{\rm cr}$.

The case (6,0.6) is a prime example of strong heating, as seen from Fig. 10 and Table V. The values for final $\langle p\rangle$ increase roughly 10% if we take the cutoff at 200 units instead of 100 units. The recycling effect works well for small $p_0$ and the distribution is clearly quite independent of $p_0$. Eventually the Landau-Zener approach starts to work and a notable peak at $p = p_0$ emerges when $p_0 > \sqrt{\Omega}$. Our ensemble sizes are clearly too small for catching the true form of this peak, but large enough to get the rest of the distribution more or less correctly. In this case the Landau-Zener approach is the way to estimate the accuracy of the simulation technique; normally the situation is reversed.

The case (10,1), presented in Fig. 11 and Table VI, is much like the (6,0.6) case, except that the larger value of $\Omega$ enhances the recycling effect and the larger value of $\Delta$ (leading to the increase of $\alpha$) increases the acceleration during the exponential decay. Hence a very long tail as a continuation of the main body of the distribution is present. The familiar peak at $p = p_0$ emerges as the adiabaticity and therefore the recycling effect becomes weak for $p_0 \gtrsim \sqrt{\Omega}$. However, as shown by Table VI, the values for $\langle p\rangle$ remain rather constant even with cutoff placed at $p = 200$. For the $p = 100$ cutoff the values for $\langle p\rangle$ fall below $p_0$, hence in order to grasp the full situation we need to increase the cutoff to 200.

The Landau-Zener approach works in the same way for the (10,1) case as it does for the (6,0.6) case: a peak at $p = p_0$ is present for all $p_0$, gaining height as $p_0$ goes from 10 to 60. The Landau-Zener theory works well for $p_0 = 35 - 45$, but for larger $p_0$ it predicts an asymmetry near the peak (also present in Fig. 10), favoring the higher momentum values. This may be due to small ensemble sizes or the breakdown of linearization argument. In the latter case it is likely that the Landau-Zener approach underestimates the acceleration at first crossing, and in reality the momentum components with $p > p_0$ are spread rather more evenly towards $p \gg p_0$. The estimate for $\langle p\rangle$ given by Eq. (37) is slightly larger than the results given in Table VI.

### B. Centrifugal barrier effects

In this subsection we extend our study to the higher partial waves, i.e., to cases with $l \neq 0$. In a previous study [9] we concluded that the kinetic energy change can be regarded roughly as constant for $l \leq l_{\rm max}$, and negligible for $l \geq l_{\rm max}$, where $l_{\rm max}$ is obtained from a semiclassical argument, as shown later. Therefore it is adequate to study only $s$-wave scattering, i.e., the $l = 0$ case. Here we shall further test and discuss this assumption.

A typical example of the level structure for the $l \neq 0$ cases is shown in Fig. 12. The effect of the repulsive $l(l+1)/R^2$ contribution to the ground-state potential is notable, but the excited state barely feels it. Since both potentials are affected, $R_{\rm cr}$ and $\alpha$ are independent of $l$. However, the slope of the excited-state potential at $R_{\rm cr}$ is no longer exactly equal to $\alpha$.

The concept of an $l_{\rm max}$ cutoff is based on a simple semiclassical argument. The wave packet loses momentum as it moves along the ground-state potential towards $R = 0$. Eventually it reaches the classical turning point $R_l \simeq \sqrt{l(l+1)}/|p_0|$ and, having lost all its kinetic energy $\sim p_0^2$, it turns back. When $R_l \simeq R_{\rm cr}$ the tide turns:

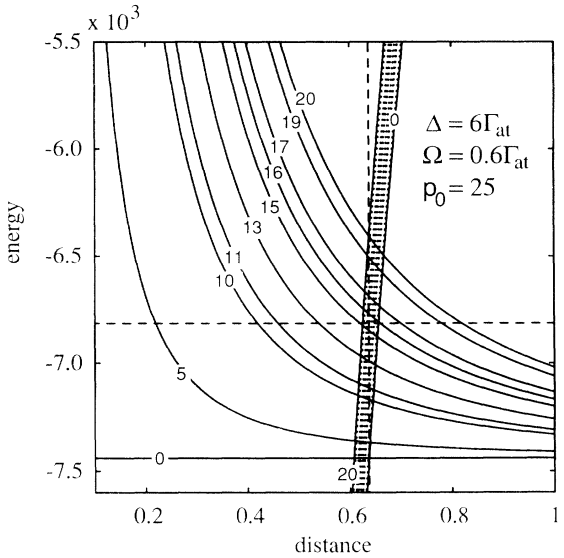


FIG. 12. The level structure for the angular-momentum study in the (6,0.6) case. The solid lines correspond to the ground-state potential surfaces, each labeled with the corresponding value of the angular-momentum quantum number $l$. The corresponding excited-state potential surfaces are drawn with dotted lines, and they form a rather solid band, which has been emphasized by using solid lines for the $l = 0$ and $l = 20$ cases (labeled). The dashed vertical line shows the position of the crossing point $R_{\rm cr}$ which remains constant. The dashed horizontal line sets the semiclassical kinetic energy for the wave packet with $p_0 = 25$ and the classical turning points $R_l$ are the points where this line intercepts the corresponding ground-state potential surfaces. In this particular case we have $l_{\rm max} \simeq 16$.

for higher $l$ the crossing is shielded as the wave packet is reflected before it can reach the crossing. Hence we have for heating $l_{\max} \simeq R_{\rm cr}|p_0|$.

For small detunings one can see strong deformation of the excited-state potential, especially for large $l$. However, we are interested in cases where the heating is strong. Then we usually have a large detuning and the deformation is small (as in Fig. 12). For small detunings heating is strong only for very small $p_0$ (Fig. 9), so that $l_{\max}$ remains small, reducing the deformation. In fact, in our model we have to go to values such as $\Delta \simeq \Gamma_{\rm at}$ and $p_0 \simeq 50$ in order to produce an example of highly deformed level structure for $l < l_{\max}$. Simulation results for that particular case (with $\Omega = \Gamma_{\rm at}$) do not show any spectacular phenomena, and we observe only negligible heating anyway.

In order to extend the Landau-Zener approach to cover the $l \neq 0$ cases we turn again to energy conservation and classical ideas. The repulsive ground state slows the wave packet, and its components with initial momentum $p$ reach the crossing carrying the momentum

$$p' = \sqrt{p^2 - \frac{l(l+1)}{R_{\rm cr}^2}}. \tag{39}$$

In practice we just replace $p_0$ with $p_0'$ in Eq. (33). For large detunings $\alpha$ is still a good approximation for the slope. As $\Delta\tilde{U}$ is independent of $l$, the energy gain due to a quantum jump is unchanged. We assume strong decay, so that the potential difference on the ground state between points $R_j$ where the jump occurred and the crossing point $R_{\rm cr}$ is negligible, thus producing no further increase in the kinetic energy during the passage from $R_j$ to the second crossing. After the second crossing the wave packet still gains some kinetic energy as it rolls down from $R = R_{\rm cr}$ to $R \gg R_{\rm cr}$. Therefore we have to invert Eq. (39) and use it on $p$ in Eq. (33); in practice this leads to a shift in the distribution towards larger $p$ with a sharp lower cutoff at small $p$.

We present the simulation results in Fig. 13 and Table VII. They correspond to the level structures presented in Fig. 12. The failure of the extended Landau-Zener approach is evident for $l \neq 0$. The cutoff at low $p$ is not as sharp as predicted by the semiclassical approach. This suggests that those wave-packet components which are excited at the second crossing advance on the excited state clearly to the region where $R \gg R_{\rm cr}$ before a quantum jump takes place. Hence they are already strongly decelerated, and in addition gain less extra kinetic energy when reemerging on the ground state at $R_j \gg R_{\rm cr}$ rather than at the immediate vicinity of $R_{\rm cr}$. The net result is a smooth tail towards $p = 0$.

At $l = l_{\max}$ the contribution of the initial momentum distribution is much less than expected from the Landau-Zener approach. The reason is clear: the coupling $\Omega$ provides a tunneling effect that enables the wave packet to reach the crossing even when it is classically forbidden. This becomes clear if we consider the wave packet moving along the lower adiabatic potential surface [which corresponds to the smaller eigenvalue of the nondiagonal Hamiltonian in Eq. (19), see Fig. 1]. Then the potential surface has a maximum at $R_{\rm cr}$, which in energy scale lies $\Omega$ units below the point where the diabatic surfaces cross. Hence the tunneling observed in the diabatic frame is in the adiabatic frame classically allowed motion through the crossing region. This feature has been confirmed with wave packets in Ref. [25] using linear level crossings. When the crossing of the potential barrier even in the adiabatic frame becomes classically forbidden, the wave-packet results show no marked ef-

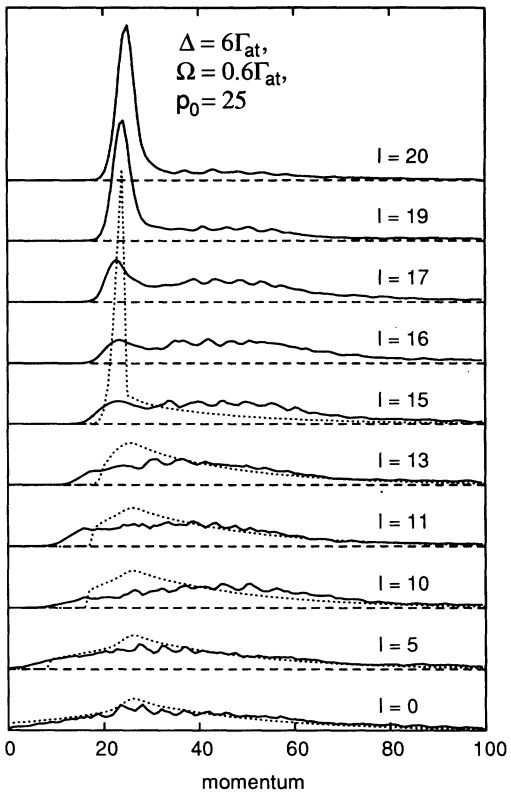


FIG. 13. The final momentum distributions for the angular-momentum study in the (6,0.6) case with $p_0 = 25$. The solid lines present the simulation results and the dotted lines stand for the Landau-Zener results from the extended model; the latter ones are given only for $l < l_{\max} \simeq 16$.

TABLE VII. The angular-momentum study for the (6,0.6) case with $p_0 = 25$. The angular-momentum quantum number is $l$, otherwise the presentation follows Table III. The data from the extended Landau-Zener approach are omitted for $l > 15$ as the crossing becomes shielded in the classical picture.

| $l$ | $\langle p\rangle_{200}$ | $\langle p\rangle$ | $\langle p\rangle_{\rm LZ}$ | $\Delta w_{200}$ | $\Delta w$ | $\Delta w_{\rm LZ}$ | $N$ | $\bar{n}$ | $\Delta n$ |
|---|---|---|---|---|---|---|---|---|---|
| 0 | 49 | 42 | 36 | 4.7 | 2.6 | 1.7 | 55 | 9.8 | 3.7 |
| 5 | 51 | 42 | 38 | 5.3 | 2.6 | 1.9 | 53 | 9.8 | 11.8 |
| 10 | 57 | 48 | 41 | 6.0 | 3.3 | 2.1 | 72 | 11.5 | 14.7 |
| 11 | 50 | 42 | 41 | 4.7 | 2.5 | 2.2 | 72 | 7.8 | 6.9 |
| 13 | 54 | 45 | 41 | 5.4 | 2.9 | 2.2 | 92 | 8.4 | 6.9 |
| 15 | 54 | 47 | 33 | 5.4 | 3.1 | 1.1 | 55 | 8.9 | 10.6 |
| 16 | 58 | 49 | | 6.1 | 3.4 | | 63 | 10.4 | 12.6 |
| 17 | 52 | 45 | | 4.9 | 2.8 | | 63 | 9.3 | 9.1 |
| 19 | 40 | 37 | | 2.7 | 1.7 | | 71 | 7.5 | 6.4 |
| 20 | 37 | 33 | | 2.3 | 1.2 | | 55 | 6.9 | 2.9 |

fects; the excitation probability merely keeps decreasing steadily and disappears eventually when the height of the barrier is much larger than $p_0^2$. This is probably due to the fact that a wave packet is a momentum distribution of finite width, rather than a $\delta$ function.

Although the extended Landau-Zener approach fails for $l \neq 0$, the use of $l_{\max}$ obtained from the classical description provides a reasonable lower estimate for heating calculations. We observe that as $l$ increases the heating is at first slightly enhanced from the value at $l = 0$ as the wave packets arrive at $R_{\rm cr}$ with reduced momentum and the adiabaticity of the crossing process is increased. The acceleration taking place between $R_j$ and $R_{\rm cr}$ also increases kinetic energy further and hence reduces the excitation probability at the second crossing. The magnitude of these enhancements, however, is not very large, just barely observable in the limits given by the statistical inaccuracy of the simulation method. Because of the power-induced lowering of the potential barrier, the heating still continues at $l > l_{\max}$ but dies off rather rapidly with increasing $l$ as the height of the barrier increases roughly as $l^2$.

In Ref. [25] a trapping of the wave packet in the potential well formed by the upper adiabatic surface was observed in addition to the barrier lowering effect. In our case this rather narrow well roughly consists of the ground state at $R < R_{\rm cr}$ and of the excited state at $R > R_{\rm cr}$. Such trapping would strongly increase the time the wave packet spends near the crossing region, and the number of quantum jumps could increase. In Table VII we see that except for $l = 0$ and $l = 20$ the standard deviation is quite large. The reason is that for other values of $l$ we observe that the number of quantum jumps in most members of the ensemble lay close to the average value $\bar{n} \lesssim 10$, but for about $\lesssim 10$ % cases the number of jumps is in the region 30–70. This changes the average very little, but clearly affects $\Delta n$. We do not observe this jump behavior in any of the $l = 0$ cases presented in the previous subsection, so it seems to be a clear $l \neq 0$ effect. The actual averages over different wave packets (in the form featured in Figs. 5 and 6) do not reveal any clear differences between $l = 0$ and $l \neq 0$ cases. There is the small peak in excited-state population at $R \simeq R_{\rm cr}$ which survives long after the main body of the wave packet has left the immediate crossing region, but it is present also for the $l = 0$ case (Fig. 5).

We can, therefore, conclude that one can use the s-wave result for $\Delta w$ and the semiclassically obtained $l_{\max}$ for producing an estimate for the total kinetic energy change. Since the simulations are tedious and time consuming, this fact is of utmost importance.

### C. Simulation statistics

For the Monte Carlo state-vector method the choice of suitable sizes for the ensembles is an important and nontrivial problem. Hence for all specific applications of the method the way the ensemble is formed and how it converges towards the density-matrix result must be addressed with care. In this subsection we discuss the problem in the context of our study.

In Tables III–VII we have given the ensemble statistics for each simulation for all the data presented. Based on previous studies [10] we have in general used $N = 50$ as the basic ensemble size, which has kept the duration of each simulation within the limits we find acceptable (less than a week depending on the workstation in question and its then current load).

In Fig. 14 we show typical quantum jump distributions. In most cases the number of jumps form a simple group around the average value. In practice the $N = 50$ is a reasonable size if the individual evolution histories for ensemble members all remain very alike. However, complications can occur. In the (10,0.2) case there is a clear switching between cases with either zero quantum jumps or one jump. In Fig. 7 the ensemble sizes were $N = 202$ for $p_0 = 10$ and $N = 278$ for $p_0 = 15$. The corresponding portions of zero jump cases are 36% and 52%. However, another simulation for $p_0 = 10$ ($N = 65$) gives 49% and the final distribution has a flat top instead of the two-peak structure. It is clear that the final distribution in the (10,0.2) and $p_0 = 10$ case is made of two peaks, one for the zero jump case and the other for the one jump case. The tail is probably formed by cases with more than one jump. Hence in order to have the correct form for the main body of the distribution we would need a truly large ensemble. Only then can the correct relative occurrence of zero and one jump cases be established with reasonable certainty.

Similarly, in the strong heating cases with large $p_0$ we know that there must be cases which preserve part of the initial wave packet. This is because the population inversion [Eq. (26)] in most cases produces a sizable reflection of the ground-state distribution on the excited state. Hence all information about the initial wave packet is destroyed only if either the ground state is fully depleted by a strongly adiabatic excitation, or the levels are strongly decoupled over the area where the ground-state wave packet happens to be when the jump takes place. In Tables III–VII the number of jumps is relatively large, and increases with the steady-state inversion. In fact,

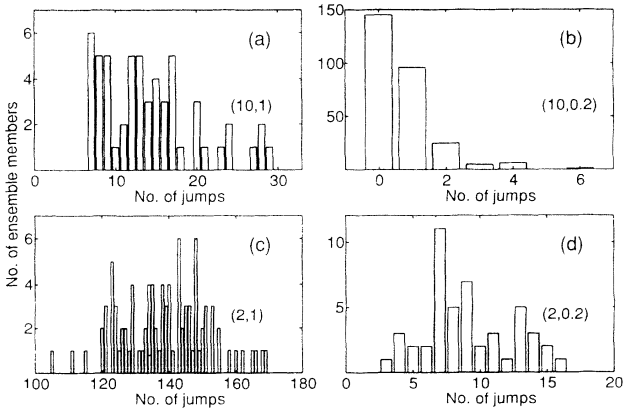


FIG. 14. Examples of the distributions for the quantum jump occurrences in ensemble members for selected simulations. The parameters are as marked in the graph; for all cases $p_0 = 15$. The statistical data are (a) $N = 56$, $\bar{n} \simeq 14$, and $\Delta n \simeq 6$; (b) $N = 278$, $\bar{n} \simeq 0.7$, and $\Delta n \simeq 0.9$; (c) $N = 92$, $\bar{n} \simeq 140$, and $\Delta n \simeq 13$; (d) $N = 48$, $\bar{n} \simeq 9$, and $\Delta n \simeq 3$.

many of the reported quantum jumps take place while the wave packet is in the steady state before or after the collision, especially when we wait for the small trapped or strongly decelerated components to emerge from the interaction region. This is especially true for the (2,1) case; the decline in $\bar{n}$ with increasing $p_0$ in Table IV is mainly due to the gradual shortening of the integration time from 0.5 to 0.35. Small ensemble sizes will tell us that we have contributions from the initial wave packet, and from the well-spread tail structure. The form of the tail is given rather well, but the exact ratio between the two possibilities can be accurately defined only with relatively large ensemble sizes which lie beyond those we have used.

We observed a clear two-case behavior also in the studies of angular-momentum states presented in the preceding subsection. There we had the number of jumps per ensemble member either roughly 10 or alternatively above 30. In the wave-packet evolution we could not see any clear two-case structure. Clearly the weaker effect ($\lesssim 10\%$) becomes hidden by the bulk behavior. However, when building the ensemble one could use the number of jumps in order to classify the wave-packet histories into two separate groups. Then we would be in a better position to study the less probable processes. This is one clear advantage of the simulation method over the standard density-matrix study, where disentanglement of different histories is not possible, unless they correspond to behavior that leads to a clear separation either in position or momentum space.

Our view is that $N = 50$ is an adequate ensemble size to determine wave-packet effects in the presence of spontaneous decay when the things we look at can be regarded as a bulk effect to which all the different histories contribute, differing only slightly from each other. As in the Feynman path integral representation of quantum mechanics, we expect all the quantum trajectories to concentrate in the vicinity of a single classical trajectory. If there were many possible but clearly separate classical trajectories, we would have to determine the quantum motion near each of them, and also the extra probabilities for picking up a certain classical trajectory. In wave-packet dynamics this would probably require $N = 500$–$5000$ members for an ensemble. We cannot always wait for the computers to create such ensembles.

## VI. DISCUSSION AND CONCLUSIONS

In this paper we have shown how it is now possible to solve the problem of ultracold atomic collisions in the presence of laser driving fields and damping due to spontaneous decay. The computation, although very considerable, is still well within the range of the capabilities of today's workstations. This has to be contrasted with a direct assault on the time-dependent density matrix, which is still out of the question [10]. We have shown that these cold collisions produce heating of the atoms that can be very significant near the saturation limit especially at the temperatures below the Doppler limit $T_D$. At temperatures around and above $T_D$ the changes in the momentum are modest compared with the initial one. This suggests that a semiclassical approach such as that used by Smith and Burnett [27] will be appropriate in this limit.

For the lower temperatures we study we have seen that the momentum spread can become very large compared to the initial one. This goes hand in hand with significant reexcitation (population recycling) and precludes any simple quantitative approach. We have, however, been able to give what we feel are sound physical pictures of these processes based partly on semiclassical notions. The results that we have presented in this article and elsewhere [8] clearly state that the Landau-Zener theory with semiclassical trajectories is the undisputed basic approach outside the population recycling region, against which all other methods should be compared. The approach also gives good physical insight into the complicated problems.

It should be emphasized that our treatment is time dependent, so many of the standard concepts of the time-independent scattering theory appear in a form which differs from the usual one. For example, bound-state resonances appear via trapping of the wave packet on the excited-state potential. At small detunings the resonances disappear due to the spontaneous decay: the bound-state structure near the continuum is dense and easily smeared out by the natural linewidth. For large detunings, however, resonances can be observed in trap loss rates [28], which arise from population exchange between two fine-structure excited states of the collisional quasimolecule at interatomic distances of the order $R \sim 100a_0$. As the states involved have very different asymptotic energies, this exchange leads to clear trap loss instead of heating. The process is very sensitive to the population of the excited state even when it is very small. Hence even negligible trapping of wave-packet components on the excited state is observed as resonance structure in the loss rates related to the fine-structure change. Detectable collisional heating, on the other hand, is a bulk effect and involves therefore the main part of the wave packet. Our results show that trapping on this scale is practically absent and hence the resonances have no visible role in the heating process.

The results of our calculations still have to be combined with models of specific experimental arrangements to obtain predictions for the velocity distributions in the presence of laser cooling and collisional heating. Our calculations provide momentum-changing cross sections for such models. We shall present elsewhere how to use the momentum distributions in the more general thermodynamical context. We are also confident that the method described here will form the basis for future work in which the sundry approximations we have made can be relaxed.

## ACKNOWLEDGMENTS

The authors thank Jinx Cooper and Paul Julienne for helpful discussions, and U.K. Engineering and Physical Sciences Research Council for support. M.J.H. acknowledges support from the Royal Society. K.-A.S wishes to thank Stig Stenholm, Research Institute for Theoretical Physics of the University of Helsinki, Academy of Finland and Suomalainen Tiedeakatemia for support.

[1] P. S. Julienne and F. H. Mies, J. Opt. Soc. Am. B **6**, 2257 (1989).
[2] A. Gallagher and D. E. Pritchard, Phys. Rev. Lett. **63**, 957 (1989).
[3] P. S. Julienne, Phys. Rev. Lett. **61**, 698 (1988).
[4] P. S. Julienne and J. Vigué, Phys. Rev. A **44**, 4464 (1991).
[5] A. M. Smith, K. Burnett, and P. S. Julienne, Phys. Rev. A **46**, 4091 (1992).
[6] Y. B. Band and P. S. Julienne, Phys. Rev. A **46**, 330 (1992).
[7] H. M. J. M. Boesten, B. J. Verhaar, and E. Tiesinga, Phys. Rev. A **48**, 1428 (1993).
[8] K.-A. Suominen, M. J. Holland, K. Burnett, and P. S. Julienne, Phys. Rev. A **49**, 3897 (1994).
[9] M. J. Holland, K.-A. Suominen, and K. Burnett, Phys. Rev. Lett. **72**, 2367 (1994).
[10] W. K. Lai, K.-A. Suominen, B. M. Garraway, and S. Stenholm, Phys. Rev. A **47**, 4779 (1993).
[11] B. M. Garraway, S. Stenholm, and K.-A. Suominen, Phys. World **6** (April), 46 (1993).
[12] P. S. Julienne, A. M. Smith, and K. Burnett, in *Advances in Atomic, Molecular and Optical Physics*, edited by D. R. Bates and B. Bederson (Academic Press, San Diego, 1993), Vol. 30, pp. 141–198.
[13] M. Trippenbach, Bo Gao, J. Cooper, and K. Burnett, Phys. Rev. A **45**, 6555 (1992).
[14] M .S. Child, *Molecular Collision Theory* (Academic, London, 1974); *Semiclassical Mechanics with Molecular Applications* (Clarendon Press, Oxford, 1991).
[15] W. H. Press, B. P. Flannery, S. A. Teukolsky, and W. T. Vetterling, *Numerical Recipes in C* (Cambridge University Press, Cambridge, England, 1988).
[16] K.-A. Suominen, B. M. Garraway, and S. Stenholm, Phys. Rev. A **45**, 374 (1992).
[17] A. Goldberg, H. M. Schey, and J. L. Schwartz, Am. J. Phys. **35**, 177 (1967).
[18] K.-A. Suominen and B. M. Garraway, Phys. Rev. A **48**, 3811 (1993).
[19] H. J. Carmichael, *An Open Systems Approach to Quantum Optics* (Springer-Verlag, Berlin, 1993).
[20] N. Gisin and I. C. Percival, Phys. Lett. A **167**, 315 (1991); J. Phys. A **25**, 5677 (1992).
[21] J. Dalibard, Y. Castin, and K. Mølmer, Phys. Rev. Lett. **68**, 580 (1992); Y. Castin, K. Mølmer, and J. Dalibard, J. Opt. Soc. Am. B **10**, 524 (1993).
[22] R. Dum, P. Zoller, and H. Ritsch, Phys. Rev. A **45**, 4879 (1992); C. W. Gardiner, A. S. Parkins, and P. Zoller, *ibid.* **46**, 4363 (1992); R. Dum, A. S. Parkins, P. Zoller, and C. W. Gardiner, *ibid.* **46**, 4382 (1992); P. Marte, R. Dum, R. Taïeb, P. D. Lett, and P. Zoller, Phys. Rev. Lett. 71, 1335 (1993).
[23] R. Loudon, *The Quantum Theory of Light*, 2nd ed. (Oxford University Press, Oxford, 1983).
[24] L. D. Landau, Phys. Z. Sowjet Union **2**, 46 (1932); C. Zener, Proc. R. Soc. London, Ser. A **137**, 696 (1932).
[25] B. M. Garraway, K.-A. Suominen, and S. Stenholm, in *Light Induced Kinetic Effects on Atoms, Ions and Molecules*, edited by L. Moi *et al.* (ETS Editrice, Pisa, 1991), pp. 129–138; B. M. Garraway and S. Stenholm, Opt. Commun. **83**, 349 (1991).
[26] B. M. Garraway and S. Stenholm, Phys. Rev. A **46**, 1413 (1992).
[27] A. M. Smith and K. Burnett, J. Opt. Soc. Am. B **8**, 1592 (1991).
[28] P. S. Julienne, K.-A. Suominen, and Y. B. Band, Phys. Rev. A **49**, 3890 (1994).